H + NO_2 Channels in the Photodissociation of HONO at 193.3 nm†

Gabriel Amaral, Kesheng Xu, and Jingsong Zhang*

Department of Chemistry, University of California, Riverside, California 92521-0403

Received: July 14, 2000; In Final Form: September 27, 2000

The H + NO_2 channels in the 193.3-nm photodissociation of jet-cooled HONO have been examined by using high-*n* Rydberg-atom time-of-flight (HRTOF) technique. Center-of-mass (CM) translational energy distribution and energy-dependent angular distribution of the photoproducts reveal that the NO_2 fragments are produced in at least three electronic states: ground $\tilde{X}^2A_1$ and excited $\tilde{A}^2B_2$ and $\tilde{B}^2B_1$ (and/or $\tilde{C}^2A_2$) states. The overall average CM product translational energy is $\langle E_T \rangle = 0.3E_{avail}$. NO_2 fragments are highly vibrationally excited in each of these electronic states, and in particular, a long vibrational progression of NO_2 bending mode in the $\tilde{A}^2B_2$ state has been observed. Branching ratios of the NO_2 electronic states are estimated: $\tilde{X}^2A_1$:$\tilde{A}^2B_2$:$\tilde{B}^2B_1$/$\tilde{C}^2A_2 \approx 0.13:0.21:0.66$. The O−H bond photodissociation of HONO from the second electronically excited singlet state B^1A' proceeds via multiple dissociation pathways. The H + $NO_2(\tilde{A}^2B_2)$ product channel is via a direct dissociation (presumably in a near-planar fragmentation geometry) and has a large translational energy release, a specific NO_2 bending vibration population (indicating a significant change of the ONO angle during dissociation), and an anisotropic product angular distribution (suggesting a short excited $\tilde{B}^1A'$ state lifetime with respect to dissociation). The H + $NO_2(\tilde{X}^2A_1)$ channel could be produced from a triplet excited state (which likely has a repulsive barrier along the O−H dissociation coordinate) following intersystem crossing or from the ground state of HONO after internal conversion. The H + $NO_2(\tilde{B}^2B_1)$ channel requires nonadiabatic processes in a planar geometry, while in nonplanar geometries, it can be directly produced from the HONO($\tilde{B}^1A'$) state, consistent with its large branching ratio.

Introduction

Nitrous acid (HONO) is an important trace species in tropospheric chemistry.[1−5] Near-ultraviolet (near-UV) photolysis of HONO generates a significant amount of OH radicals at sunrise after nighttime accumulation and initiates the chain reactions in photochemical smog formation in air polluted urban areas.[1−5] Accurate photochemical kinetic and mechanistic information of HONO is essential for understanding its roles in atmospheric chemistry. For example, the branching ratios of the dissociation channels OH + NO and H + NO_2 are important for addressing the OH production at sunrise and NO to NO_2 conversion under conditions of low ozone concentrations.

Near-UV and UV absorption spectra of HONO consist of (i) a diffuse structured band in the 300−390 nm region and (ii) a broad structureless band from 270 nm to below 180 nm, peaking at ∼210 nm.[5−8] On the basis of the electronic configuration of the ground-state HONO, ...$(8a')^2(1a'')^2(9a')^2(2a'')^2(10a')^2(3a'')^0$, the first absorption band in the near-UV region has been attributed to the $10a'(n_O) \rightarrow 3a''[\pi^*(N{=}O)]$ transition (promotion of an in-plane lone-pair *p* electron on the terminal oxygen atom to the first antibonding π^* orbital primarily located on the terminal N═O) and corresponds to the electronic excitation to the first singlet excited state ($\tilde{A}^1A'' \leftarrow \tilde{X}^1A'$).[8−13] This band consists of vibrational progression (2_0^n) in the ν_2 mode (primarily the terminal N═O stretch), indicating a significant change in the terminal N═O bond length in the $\tilde{A}^1A'' \leftarrow \tilde{X}^1A'$ transition.[5c,8−13] The second absorption band has been attributed to the $2a''(\pi_{nb,O}) \rightarrow 3a''[\pi^*(N{=}O)]$ transition [promotion of a lone-pair 2pπ electron on the OH oxygen atom to the π^*(N═O) orbital], and corresponds to the excitation to the second singlet excited state ($\tilde{B}^1A' \leftarrow \tilde{X}^1A'$), although the third singlet excited state ($\tilde{C}^1A''$, via the $9a' \rightarrow 3a''$ transition) might be involved as well.[9] The electronic energy levels of HONO and their correlations (in a C_s point group) to the H + NO_2 and OH + NO product channels are shown in Figure 1.[9,14] The possible dissociation channels are listed as follows: [9,15−17]

$$\text{HONO}(\tilde{X}^1A') (+h\nu) \rightarrow \text{OH}(X^2\Pi) + \text{NO}(X^2\Pi) \quad \Delta H_0^\circ = 48.0 \text{ kcal/mol} \quad (1a)$$

$$\rightarrow \text{OH}(A^2\Sigma) + \text{NO}(X^2\Pi) \quad \Delta H_0^\circ = 140.6 \text{ kcal/mol} \quad (1b)$$

$$\rightarrow \text{H}(^2S) + \text{NO}_2(\tilde{X}^2A_1) \quad \Delta H_0^\circ = 77.5 \text{ kcal/mol} \quad (2a)$$

$$\rightarrow \text{H}(^2S) + \text{NO}_2(\tilde{A}^2B_2) \quad \Delta H_0^\circ = 105.3 \text{ kcal/mol} \quad (2b)$$

$$\rightarrow \text{H}(^2S) + \text{NO}_2(\tilde{B}^2B_1) \quad \Delta H_0^\circ = 117.9 \text{ kcal/mol} \quad (2c)$$

$$\rightarrow \text{H}(^2S) + \text{NO}_2(\tilde{C}^2A_2) \quad \Delta H_0^\circ = 120.0 \text{ kcal/mol} \quad (2d)$$

Photodissociation of the HONO $\tilde{A}^1A''$ state has been extensively studied.[10−13,18−24] Both channels 1a and 2a are energeti-

† Part of the special issue "Harold Johnston Festschrift".

* To whom all the correspondence should be sent. Fax: 909-787-4713. E-mail: jszhang@ucrac1.ucr.edu. Also at Air Pollution Research Center, University of California, Riverside.

10.1021/jp002521e CCC: $20.00
Published on Web 11/29/2000

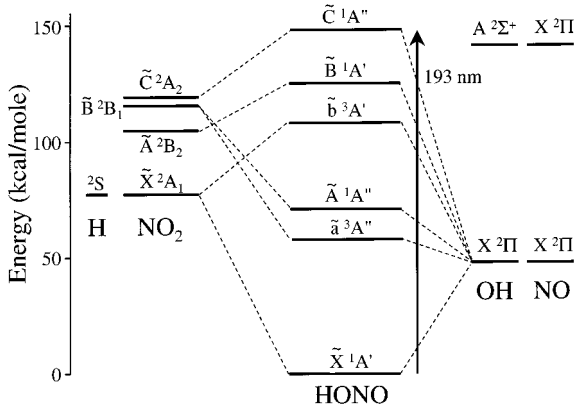

Figure 1. Energy level and correlation diagram of the HONO system and energetically possible dissociation channels (assuming a coplanar fragmentation geometry). The situations for nonplanar geometries are also discussed in the text. Upper limits of the adiabatic energies of the HONO $\tilde{A}^1A''$ and $\tilde{B}^1A'$ states are derived from absorption spectra,[5,27] and the energy levels of other electronically excited states are scaled on the basis of ref 9. Energetics of the product channels are derived from thermodynamic data in ref 15 and NO_2 electronic energies from refs 16 and 17. The energy levels are drawn to scale.

cally possible in the near-UV absorption band. The $OH(X^2\Pi)$ + $NO(X^2\Pi)$ channel (1a) has been identified as the major product channel with a nearly unit quantum yield, although recent experimental evidence indicated that the H + NO_2 channel (2a) possibly has a nonnegligible branching ratio at wavelengths shorter than its threshold of 369 nm.[6,25] Channel 1a has been shown to occur via a fast vibrational predissociation.[10−13,18−23] State-resolved laser-induced fluorescence (LIF) measurements have shown that the OH fragment is rotationally and vibrationally cold (with its half-filled pπ orbital preferentially oriented in the plane of rotation) and translationally hot (with an anisotropy parameter $\beta \sim -1$, indicating a transition dipole moment perpendicular to the molecular plane and a prompt and planar dissociation pathway).[18−21] The NO fragment, however, has significant internal energy with a inverted vibrational and rotational state population,[21,22] suggesting a strong coupling between the terminal N═O bond and the N−O dissociation coordinate. A dissociation lifetime of ∼100 fs (20 fs for 2_0^0 and 100 fs for 2_0^3, increasing with excitation in the excited-state N═O stretch) has been inferred from vector correlation studies.[23] Ab initio quantum mechanical calculations have indicated that the Franck−Condon region of the Ã-state potential energy surface (PES) has a potential well along the terminal N═O coordinate and a small barrier to dissociation along the central O−N coordinate.[10−13] Classical trajectory and quantum dynamics calculations on the Ã state surface have confirmed many of the experimental results.[10−13]

There is little information on photodissociation dynamics of the $\tilde{B}^1A'$ state. Only a few experiments have been carried out at 193.3 nm and at 212, 218, and 220 nm, and they have focused on the OH + NO channels.[7,26,27] OH product vector correlation, Doppler profiles, and energy distribution indicate a large anisotropy and fast dissociation on the B̃ state (in the order of femtoseconds). With this prompt dissociation mechanism, the measured anisotropy parameter β of ∼1.3 indicates that the $\tilde{B}^1A' \rightarrow \tilde{X}^1A'$ transition moment lies in the molecular plane and has a ∼35° angle with the OH recoil velocity (the dissociating N−O bond).[26,27] A nonplanar equilibrium geometry in the B̃ state has been proposed (due to removal of an out-of-plane pπ electron on the O atom in the $\pi-\pi^*$ transition).[26,27] Upon vertical excitation, the OH moiety of the B̃-state HONO could undergo an out-of-plane motion, with a change in dihedral angle and excitation in out-of-plane torsion ν_6.[26,27] In addition, the vector correlation studies have revealed that, in this heterolitic N−O dissociation, the OH fragment is ejected with its plane of rotation (which contains the half-filled pπ orbital) preferentially aligned perpendicular to the recoil direction (i.e., with a propeller-type motion).[26,27] An OH(A) + NO channel has been observed at 193.3 nm with a small quantum yield of 10^{-5}, and the OH(A) rotational distribution can be described by a statistical dissociation model.[7]

The H + NO_2 channels (2a−d) have not been directly observed before. Symmetry considerations indicate that, in coplanar fragmentation pathways (C_s point group), the $\tilde{A}^1A''$ HONO correlates adiabatically with the second electronically excited-state $NO_2(\tilde{B}^2B_1)$, the $\tilde{B}^1A'$ HONO correlates with the first excited-state $NO_2(\tilde{A}^2B_2)$, and the $\tilde{C}^1A''$ HONO correlates to $NO_2(\tilde{C}^2A_2)$ (shown in Figure 1). The electronic configurations of NO_2 are as follows:[14,17] $...(1a_2)^2(4b_2)^2(6a_1)^1(2b_1)^0$ $\tilde{X}^2A_1$; $...(1a_2)^2(4b_2)^1(6a_1)^2$ $\tilde{A}^2B_2$; $...(1a_2)^2(4b_2)^2(2b_1)^1$ $\tilde{B}^2B_1$; and $...(1a_2)^1(4b_2)^2(6a_1)^2$ $\tilde{C}^2A_2$. With the plane of HONO chosen as the symmetry plane of the NO_2 fragment in the C_s point group and thus assigned as the *yz* plane for NO_2, the $^2B_2$ is then reduced to A′ and $^2B_1$ to A″ in the C_s symmetry.[14] At 193.3 nm, HONO is promoted to the singlet $\tilde{B}^1A'$ state in the spin-conserving photoexcitation.[5,7,9] As $HONO(\tilde{B}^1A')$ correlates adiabatically with H + $NO_2(\tilde{A}^2B_2)$ in a planar geometry, productions of $NO_2(\tilde{X}^2A_1)$, $NO_2(\tilde{B}^2B_1)$, or $NO_2(\tilde{C}^2A_2)$ from $HONO(\tilde{B}^1A')$ dissociation would therefore involve nonadiabatic processes. For example, the ground-state $NO_2(\tilde{X}^2A_1)$ correlates adiabatically in the planar geometry with the ground-state $HONO(\tilde{X}^1A')$ and the second excited triplet $\tilde{b}^3A'$ state, photodissociation of $HONO(\tilde{B}^1A')$ to $NO_2(\tilde{X}^2A_1)$ requires intersystem crossing with the $\tilde{b}^3A'$ surface via spin−orbit couplings or internal conversion to the ground state $\tilde{X}^1A'$ via vibronic interactions. Potential energy curves of the $\tilde{X}^1A'$ ground state and singlet and triplet excited states of HONO have been examined by ab initio calculations (restricted in the planar geometry), and the excited-state surfaces are shown to be not purely repulsive or have substantial energy barriers along the H−ONO coordinate.[9] When nonplanar dissociation pathways are considered, however, the $NO_2(\tilde{B}^2B_1)$ product correlates adiabatically with the $\tilde{B}^1A'$ HONO instead, and $NO_2(\tilde{A}^2B_2)$ with the $\tilde{A}^1A''$ and $\tilde{b}^3A'$ states of HONO, $NO_2(\tilde{X}^2A_1)$ with $\tilde{X}^1A'$ and $\tilde{a}^3A''$ HONO, and $NO_2(\tilde{C}^2A_2)$ with $\tilde{C}^1A''$ HONO. Consequently, productions of NO_2 in $\tilde{X}^2A_1$, $\tilde{A}^2B_2$, and $\tilde{C}^2A_2$ from nonplanar $HONO(\tilde{B}^1A')$ dissociation require nonadiabatic processes.

It is difficult to identify the H + NO_2 channels by using traditional methods to monitor the NO_2 products, as these techniques are severely hindered by the large background of NO_2 that is in equilibrium with HONO under laboratory conditions. In this work, we utilized a high-*n* Rydberg-atom time-of-flight (HRTOF) technique to directly detect and study the H-atom product channels. HONO molecules were cooled in a supersonic jet and photodissociated at 193.3 nm. H-atom TOF spectra were obtained and yielded product translational energy distribution, providing nascent internal state distribution of the NO_2 fragments. This work reports the first direct observation and measurement of the H + NO_2 channels in the UV photodissociation of HONO.

Experimental Section

The HRTOF technique, pioneered by Welge and co-workers, was utilized in this study and has been described previously.[28−30] A pulsed molecular beam was produced by expanding HONO

in Ar gas mixture (at a total pressure of 120 kPa) from a HONO generator into the source chamber through a pulsed nozzle (General Valve, Series-9) operating at 20 Hz with a 300 μs pulse width. The molecular beam was differentially pumped and collimated by a 1-mm diameter skimmer located 3.0 cm from the nozzle; 4.6 cm further downstream, the molecular beam was crossed with a 193.3-nm UV photolysis laser beam that was a portion of the output from an ArF excimer laser (Lambda-Physik EMG 101). The ArF laser beam (with typical 5−10-mJ energy) was focused with a quartz lens of ∼70 cm focal length. This radiation could be polarized with a 10-plate stack of quartz slides placed at the Brewster's angle, resulting in ∼95% polarization. Hydrogen atoms produced from photodissociation of HONO were excited by 121.6-nm Lyman-α radiation. This vacuum-UV radiation was generated by tripling the 364.7-nm radiation [doubled output from a Nd:YAG pumped dye laser (Lambda-Physik 3002)] in Kr and was focused into the interaction region by a MgF_2 lens. The H atoms were further excited from the 2^2P level to a high-*n* Rydberg level ($n \sim 40-90$) by the doubled output from another Nd:YAG pumped dye laser (Laser Analytical System 2051). Background ions (generated by photolysis or probe laser beams) were removed by a small negative potential applied below the interaction region and thus were prevented from reaching the detector. The high-*n* Rydberg states were radiatively metastable and stayed highly excited for many tens of microseconds while they drifted with their nascent velocities to a microsphere plate detector (El-Mul Technologies). Upon arrival at the detector, the excited atoms were efficiently field-ionized as they passed a wire mesh, and they were then detected as ions. The ion signals were amplified by a fast preamplifier (Phillips Scientific 6950). TOF spectra were recorded and averaged by using a multichannel scaler (EG&G, Turbo MCS) and were stored on a computer. The flight distance was calibrated by photodissociating HCl, and the nominal flight length was 37.1 cm. The dwell time used on the MCS was 20 ns and typically 10 000 channels were recorded. The accumulated TOF spectra shown in this work usually represent 200−400 thousand laser firings.

The HONO gas sample was prepared by reaction of aqueous solutions of $NaNO_2$ and H_2SO_4 in a HONO gas generator, which is based on the designs of Ning and Pfab[31] and Marshall and Midgeley.[32] A schematic representation of this HONO generator is shown in Figure 2. The generator was essentially a glass vessel of ∼25-cm length and ∼ 4-cm diameter. A small compartment (∼35 mL) was attached underneath the bottom of the reaction vessel in case of a liquid leak through the ceramic frit due to gas-sample pressure buildup. The reactants' aqueous solutions (5 M H_2SO_4 and 5 M $NaNO_2$) were continuously pumped into the generator through two separate glass inlets by a two-channel peristaltic pump with ∼5 mL/min flow rate. A second single-channel peristaltic pump was used to continuously remove the waste (with a pumping speed of ∼10 mL/min) to maintain a constant level of solution inside the generator. An extra waste outlet was connected to a vacuum line through a two-way valve, which was open only when pressure increased inside the vessel. Argon carrier gas entered the HONO generator from the bottom through the frit and bubbled through the liquid sample. The whole system was kept at room temperature. The HONO/NO/NO_2/H_2O/Ar mixture exited the HONO producer through a liquid-droplet trap compartment, and then passed through a 5-cm long glass drying tube filled with $CaCl_2$ as desiccant. Some amount of H_2O was still present in the sample. Since HONO tends to decompose catalytically on contact with metal surfaces, the HONO gas mixture was transported by glass and Telfon

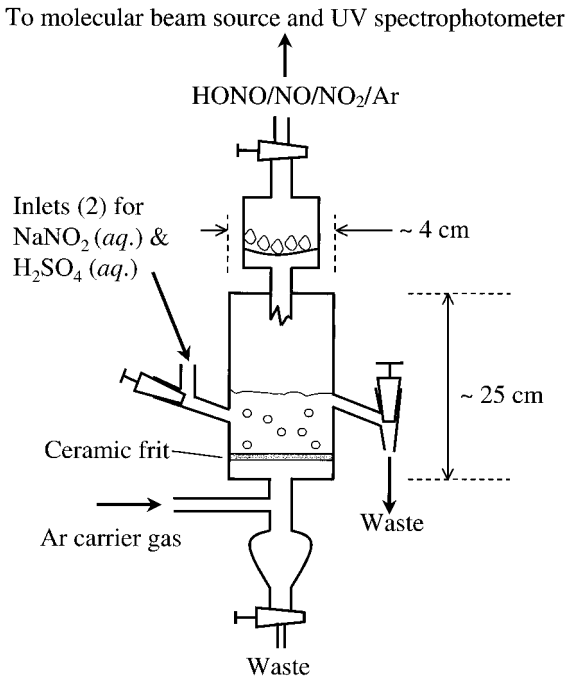

Figure 2. Schematic diagram of the HONO generator, which was based on the designs of Ning and Pfab (ref 31) and Marshall and Midgley (ref 32) and has incorporated our modifications.

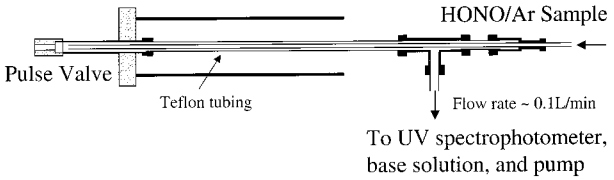

Figure 3. Schematic diagram of the flow system of the HONO sample into the molecular beam.

tubing and fittings and delivered right behind the pulsed nozzle in a flow delivery system (Figure 3). This flow system (with a constant flow rate of ∼0.1 L/min) significantly reduced the residence time of the gas sample inside the metal nozzle body and thus minimized the decomposition of HONO. No observable loss of HONO was detected by near-UV absorption spectra before and after feeding into the molecular beam nozzle source. The composition of the gas mixture in the molecular beam was examined by using a quadrupole mass spectrometer (UTI-100C) downstream. HONO ($m/e = 47$) was clearly identified, along with significant amount of NO, NO_2, and H_2O. Production of HONO was also confirmed by its characteristic near-UV absorption spectrum.[5] During the experiments, the concentrations of HONO (0.5−1%) and NO_2 in the gas mixture were continuously monitored in a 10-cm fused silica cell at the end of the gas flow system (after the beam nozzle source) by using the UV spectrophotometer (Varian DM 100S). Optimum conditions were achieved with a total gas pressure of 120 kPa and a gas flow of ∼0.1 L/min.

Population ratio of *trans*-HONO and *cis*-HONO isomers (with *trans*-HONO being more stable by ∼0.65 kcal/mol) is ∼3.25 at 277 K,[5c] and this ratio is essentially unchanged even after supersonic expansion.[23] Therefore, *trans*-HONO was treated as the major HONO isomer in this study. Although HNO_3 was considered as a possible impurity from this HONO generator,[31,32] it was not favored under the continuous flow conditions in our setup and was not identified in the quadrupole mass spectrometer. Additional experiment of 193.3-nm photolysis of HNO_3 was carried out. The H-atom TOF spectrum of HNO_3, primarily

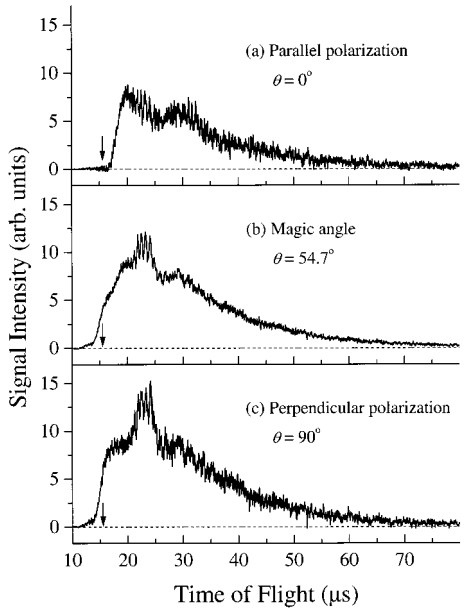

Figure 4. H-atom TOF spectrum of 193.3-nm photodissociation of HONO, with the polarization **E** vector of the photolysis radiation: (a) parallel to the TOF axis, ||, $\theta = 0°$; (b) at magic angle, $\theta = 54.7°$; and (c) perpendicular to the TOF axis, ⊥, $\theta = 90°$. The ArF laser power used was typically 5 mJ/pulse for polarized and <10 mJ/pulse for unpolarized. The signals have been normalized to the same laser power (5 mJ) and laser shots. The arrow indicates the fastest possible H atom from one-photon dissociation of HONO at 193.3 nm.

due to multiphoton processes,[33] had a very different shape compared to that from HONO photodissociation (at the same photolysis energy). Photolysis of H_2O at 193.3 nm was also studied separately. Due to the small absorption cross-section of H_2O at 193.3 nm, its photolysis would produce only a small single peak [corresponding to H + OH($X^2\Pi$, $v = 0$)] with product translational energy $E_T = 30$ kcal/mol,[34] and this peak was not identified in the TOF spectrum of HONO.

Results

H-atom TOF spectra of 193.3-nm photodissociation of HONO are shown in Figure 4. To correct for background, spectra were taken with molecular beam alternately on and off while all the other experimental conditions were kept the same. Despite a large absorption cross-section ($\sigma \sim 10^{-18}$ cm^2) of HONO at 193.3 nm,[5a,7] the signal level of the H-atom TOF spectra was low and required an extensive signal averaging, indicating small branching ratios of the H + NO_2 channels. TOF measurements were carried out with the 193.3-nm photolysis radiation unpolarized and linearly polarized [parallel (||, $\theta = 0°$) and perpendicular (⊥,$\theta = 90°$) with respect to the TOF axis]. The TOF spectra for || and ⊥ polarization (Figure 4a,c) have been corrected for the imperfect polarization of the stacked-plate polarizer. Since the linearly polarized photolysis radiation preferentially excites HONO molecules with their electronic transition dipole moments parallel to its electric vector **E**, H-atom product angular distributions can be obtained in the polarization studies.[35] The angular-dependent TOF spectra of the photofragment are described by[35]

$$I(t,\theta) = \frac{1}{4\pi} I(t)[1 + \beta(t)\, P_2(\cos\theta)] \qquad (3)$$

where β is the anisotropy parameter ($-1 \le \beta \le 2$), θ is the angle between the **E** vector of the polarized laser radiation and the recoiling velocity vector of the H-atom product (the direction of detection), and $P_2(\cos\theta)$ is the second Legendre polynomial. Due to the small H-atom mass, center-of-mass (CM) velocities of the H atoms (those with CM product translational energy $E_T > 2$ kcal/mol) are much larger than the laboratory velocity of the parent molecule (velocity of the CM). Therefore, CM and laboratory frames are essentially the same in this study; i.e., the laboratory velocity and CM velocity of the H atoms are the same, and the angle θ, defined in the CM frame, is effectively the same as that in the laboratory frame. Similar to eq 3, CM differential cross-sections of the photofragments, i.e., angular-dependent product CM translational energy distributions, are expressed as[35,36]

$$P(E_T,\theta) = \frac{d^3\sigma}{dE_T\, d\Omega} = \frac{1}{4\pi} P(E_T)[1 + \beta(E_T)\, P_2(\cos\theta)] \qquad (4)$$

where $P(E_T)$ is the angle-integrated product CM translational energy distribution, i.e., the integrated differential cross-sections over scattering angles. The $P(E_T,\theta)$ distributions can be obtained by appropriate transformation of the TOF spectra $I(t,\theta)$ (with a factor of t^3).[29] Note that the β parameter can be energy-dependent.

At magic angle ($\theta_m = 54.7°$), the TOF spectrum is independent of β; i.e., $I_m(t) = (1/4\pi)I(t)$. The magic-angle TOF spectrum can be obtained from the TOF spectra at $\theta = 0°$ (||) and $\theta = 90°$ (⊥) by $I_m(t) = [I_{||}(t) + I_\perp(t)]/3$. $I_m(t)$ can also be derived from the TOF spectrum of unpolarized 193.3-nm radiation, $I_{unpol}(t)$, by using $I_{unpol}(t) = (1/4\pi)I(t)[1 + \beta(t)/4]$. $\beta(t)$ is calculated from $\beta(t) = 2[I_{||}(t) - I_\perp(t)]/[I_{||}(t) + 2I_\perp(t)]$. The magic-angle TOF spectra obtained by combining the || and ⊥ TOF spectra and by correcting the unpolarized spectrum are essentially identical (after normalization of the laser power), which indicates proper treatments of the TOF spectra of different polarized photolysis radiation, the correction for the imperfect polarization of the polarizer, and the anisotropy parameter. The magic-angle TOF spectrum from the average of these two approaches is shown in Figure 4b.

The $P(E_T,\theta)$'s for the three polarization angles of the photolysis radiation, $P_{||}(E_T)$, $P_m(E_T)$, and $P_\perp(E_T)$, are converted from the TOF spectra in Figure 4a−c and are shown in Figure 5a−c, respectively.[29] The magic-angle $P_m(E_T)$ is proportional to $P(E_T)$ [$P_m(E_T) = (1/4\pi)P(E_T)$], and is independent of β and θ. Thus, $P_m(E_T)$ (in Figure 5b) is treated as $P(E_T)$ for calculation of translational energy release and relative branching ratios of the different product channels. CM product translational energy, E_T, is related to the internal energy of the NO_2 fragment, $E_{int}(NO_2)$, by conservation of energy:[28−30]

$$E_T = h\nu - D_0(\text{H−ONO}) - E_{int}(NO_2) \qquad (5)$$

where $h\nu$ is the photon energy and D_0(H−ONO) is the O−H bond energy. Internal energy of the HONO parent molecule is negligible due to supersonic cooling. The $P(E_T)$ distribution thus reflects the nascent internal energy distribution of the NO_2 photofragment. The energy threshold of channel 2a is 77.5 kcal/mol,[15] corresponding to a maximum available energy $E_T = 70.4$ kcal/mol, as indicated in the $P(E_T)$'s in Figure 5. The corresponding E_T onsets of the electronically excited NO_2 channels 2b−d are also marked in Figure 5. The energy-dependent anisotropy parameter β is calculated by using

$$\beta(E_T) = 2[P_{||}(E_T) - P_\perp(E_T)]/[P_{||}(E_T) + 2P_\perp(E_T)] \qquad (6)$$

and is shown in Figure 5d.

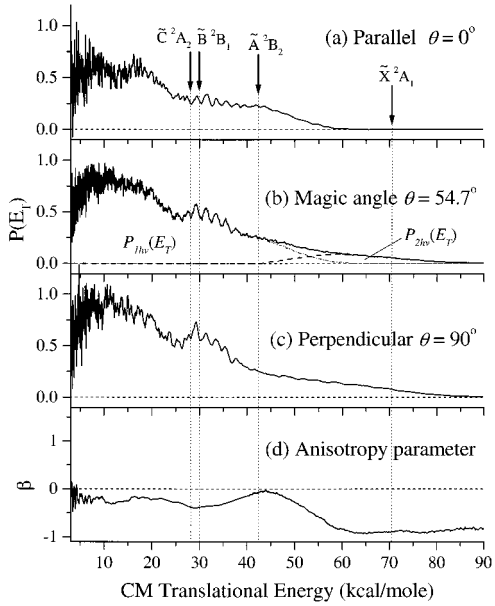

Figure 5. Product CM translational energy distributions, $P(E_T)$'s, derived from the TOF spectra in Figure 4, with 193.3-nm photolysis radiation polarization: (a) parallel to the TOF axis; (b) at magic angle; (c) perpendicular to the TOF axis; and (d) energy-dependence anisotropy parameter β. The $P(E_T)$ distributions have been normalized to the same scale. Onsets of the H + NO_2 channels are marked. Note that both $P(E_T)$'s and β have contribution from two-photon dissociation. In b, the deconvoluted one-photon component, $P_{1h\nu}(E_T)$, and two-photon component, $P_{2h\nu}(E_T)$, are plotted in dot and dash lines, respectively. See the text for details.

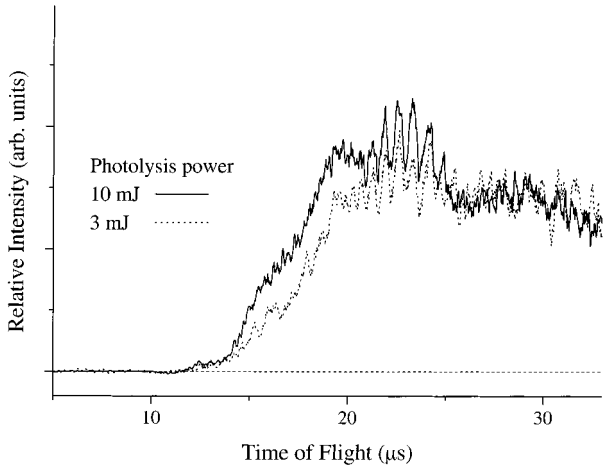

Figure 6. TOF spectra of HONO photodissociation at 193.3 nm at different laser power. The spectra are scaled to the same maximum.

The H-atom TOF spectra are complicated by a small amount of signals (starting in the region of 12−15 μs) that are faster than the maximum kinetic energy release of the H + NO_2 products (Figure 4). This fastest portion has a slope that differs from the rising edge after 15 μs in the TOF spectra, and more importantly, it has a distinctly different angular distribution ($\beta \approx -0.9$, from $E_T \sim 63$ kcal/mol to the maximum available energy in one-photon dissociation $E_T = 70.4$ kcal/mol, and to $E_T > 90$ kcal/mol, in Figure 5d). Single-photon dissociation of internally hot HONO molecules is not the source of the fast H atoms, as the observed extra energy in the fast H atoms is much larger than the possible initial internal energy of the HONO molecules in the supersonic beam. These fast signals are due to multiphoton dissociation of HONO or its clusters, which is also confirmed by photolysis power dependence (Figure 6). The H-atom TOF spectra shown in Figure 4 were taken with the photolysis laser power lowered to ~5 mJ in order to reduce the two-photon signals. In addition, the early portion of the pulsed molecular beam was used to minimize the contribution of clusters.

The β parameter remains at a nearly constant value of ~ -0.9 (the value of the two-photon component) from beyond 90 kcal/mol to ~63 kcal/mol; it then gradually increases from ~ -0.9 at $E_T \sim 63$ kcal/mol to ~0 at ~43 kcal/mol (Figure 5d). This change in β suggests that there are two product channels in this region. Since H + $NO_2(\tilde{X}^2A_1)$ (channel 2a) is the only energetically possible channel from one-photon dissociation in this energy region, the increase of the overall β indicates that the contribution of channel 2a, which has a β value ≥ 0, starts around $E_T \sim 63$ kcal/mol and increases to the maximum near 43 kcal/mol, while the contribution of the two-photon channel decreases. In the E_T region of 43−70.4 kcal/mol, $P(E_T) = P_{2h\nu}(E_T) + P_{1h\nu}(E_T)$, and the overall β is the weighted sum, $\beta(E_T) = \chi_{2h\nu}(E_T)\beta_{2h\nu} + \chi_{1h\nu}(E_T)\,\beta_{1h\nu}$, with $\chi_{ih\nu}(E_T) = P_{ih\nu}(E_T)/P(E_T)$.[36] Assuming constant β for the individual channels and using $\beta_{2h\nu} = -0.9$ and $\beta_{1h\nu} \approx 0$ (the lower limit), one can solve for $P_{2h\nu}(E_T)$ and $P_{1h\nu}(E_T)$. The deconvoluted components are plotted in Figure 5b. Note that this result is based on the lower limit $\beta_{1h\nu} \approx 0$, which gives a lower limit of the contribution of the two-photon component. The above procedure, however, should capture the general feature of the two-photon component, and in particular, contribution of the two-photon photodissociation at $E_T > 63$ kcal/mol is unambiguous, as it is the only channel in this high-energy region.

The most likely source of the fast H-atoms is sequential secondary photodissociation of OH radicals generated from 193.3-nm photolysis of HONO. $OH(X^2\Pi)$ + $NO(X^2\Pi)$ (1a) is the major channel in the primary photodissociation, and $OH(X^2\Pi)$ could be readily excited to a repulsive $^2\Sigma^-$ state by another 193.3-nm photon via a perpendicular transition and promptly dissociate into H + $O(^3P)$ with a β value of -1.[37] The observed strong anisotropy ($\beta \approx -0.9$) of the two-photon component is in agreement with this mechanism. Furthermore, the shape of the $P_{2h\nu}(E_T)$ distribution (peaking at ~63 kcal/mol) is consistent with the H + $O(^3P)$ product translational energy release from 193.3-nm photodissociation of $OH(X^2\Pi)$ radicals that are produced largely in vibrational state $\nu = 0$ and 1 and with $\beta \approx 1.3$ in the photolysis of HONO.[26,27] Although conversion of the TOF spectrum into $P(E_T)$ is based on NO_2 as the counterfragment, it can essentially apply for the two-photon component (with O atom as the countermass), since the H-atom mass is much smaller than that of O and NO_2 and the difference in conversion is negligible.

The $P(E_T)$ distribution and β parameter of 193.3-nm photodissociation of HONO, with the two-photon contribution removed, are shown in Figure 7. Note that for the H + $NO_2(\tilde{X}^2A_1)$ channel, β is chosen to be 0 (i.e., the lower limit). For $E_T \leq 70.4$ kcal/mol (maximum available energy), several distinct regions can be identified in the TOF spectra, the $P(E_T)$ distributions, and in particular, the energy-dependent β parameter (Figures 4, 5, and 7). It seems that, besides the fast two-photon channel, several product channels are present, most likely corresponding to different electronic states of NO_2. The first one starts at ~15.5 μs and continues until the pronounced break at ~20 μs in the TOF spectra. The H + $NO_2(\tilde{X}^2A_1)$ channel is unambiguously identified in this region (E_T from 70.4 to 43 kcal/mol). The second region starts at ~20 μs ($E_T \sim 43$ kcal/mol) with a different slope from that of the first region in the TOF spectra, a resolved vibrational structure, and a significant

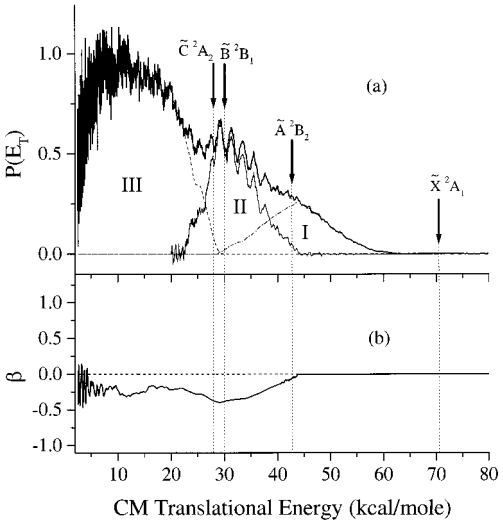

Figure 7. (a) One-photon $P_{1h\nu}(E_T)$ (from Figure 5b) and its deconvolution into three H + NO_2 product channels. The onsets of the H + NO_2 channels are marked. The $P_i(E_T)$'s in regions I, II, and III correspond to the H + $NO_2(\tilde{X}^2A_1)$, H + $NO_2(\tilde{A}^2B_2)$, and H + NO_2-$(\tilde{B}^2B_1)$ and/or H + $NO_2(\tilde{C}^2A_2)$ channels; (b) β parameter for one-photon dissociation of HONO (derived by removing the two-photon component from Figure 5d). See the text for details.

change of β. Since the threshold of the $NO_2(\tilde{A}^2B_2)$ product lies at $E_T = 42.6$ kcal/mol, the second region likely corresponds to the H + $NO_2(\tilde{A}^2B_2)$ channel. The third region begins with an abrupt change of slope in the TOF spectra and a change of β at $\sim$25 μs ($E_T \sim 30$ kcal/mol), around which the $\tilde{B}^2B_1$ and/or $\tilde{C}^2A_2$ states of NO_2 start.

The observed $P(E_T)$ distribution is thus a sum of these dissociation pathways, and the energy-dependent β is due to these multiple channels that have different β parameters and different energy-dependent branching ratios.[36] Accordingly, the overall $P(E_T)$ distribution and β can be expressed as[36]

$$P(E_T) = \sum_i^n P_i(E_T) \tag{7}$$

$$\beta(E_T) = \sum_i^n \chi_i(E_T)\beta_i \tag{8}$$

where $P_i(E_T)$ and β_i are for the ith channel and $\chi_i = P_i(E_T)/P(E_T)$ is the branching fraction of the ith channel (with $\sum_i^n \chi_i(E_T)=1$). Equations 7 and 8 can be readily derived from eq 4, with the assumption that the overall differential cross-sections are the simple sum (with no coherent interference) of those of the individual channels. The H + $NO_2(\tilde{X}^2A_1)$ channel starts from $E_T = 70.4$ kcal/mol, with a $\beta \approx 0$ (the lower limit). Starting from the threshold region of H + $NO_2(\tilde{A}^2B_2)$ ($E_T = 42.6$ kcal/mol), the overall β decreases from $\sim$0 and reaches the minimum of -0.4 at $E_T \sim 30$ kcal/mol (Figure 7b). This indicates that contribution of $NO_2(\tilde{A}^2B_2)$ increases to the maximum, while that of $NO_2(\tilde{X}^2A_1)$ decreases to the minimum and becomes insignificant below 30 kcal/mol. As the H + $NO_2(\tilde{B}^2B_1)$ channel opens at $E_T = 30.0$ kcal/mol and the H + $NO_2(\tilde{C}^2A_2)$ channel at 27.9 kcal/mol, the "turn-around" or increase of the β parameter from $E_T < 30$ kcal/mol is most likely caused by the increasing contribution of the H + $NO_2(\tilde{B}^2B_1)$ and/or $NO_2(\tilde{C}^2A_2)$ channels, rather than the H + $NO_2(\tilde{X}^2A_1)$ channel. It is difficult to separate the individual contributions of $NO_2(\tilde{B}^2B_1)$ and $NO_2(\tilde{C}^2A_2)$. Below $E_T < 22$ kcal/mol, β stays effectively at an average value of -0.2, which implies that the branching ratio of the H + $NO_2(\tilde{A}^2B_2)$ channel becomes negligible. Interestingly, the β value always changes drastically near the onsets of new product channels: at $\sim$43 kcal/mol for $NO_2(\tilde{A}^2B_2)$ and at $\sim$30 kcal/mol for $NO_2(\tilde{B}_2B_1)$ or $NO_2(\tilde{C}^2A_2)$. Assuming a constant β value for each individual channel and using $\beta \cong 0$ for $NO_2(\tilde{X}^2A_1)$, -0.4 (the observed minimum) for $NO_2(\tilde{A}^2B_2)$, and -0.2 for $NO_2(\tilde{B}^2B_1)$ and/or $NO_2(\tilde{C}^2A_2)$, the relative contribution, $P_i(E_T)$, of each of these electronic states can be deconvoluted by using eqs 7 and 8, and they are shown in the three regions in Figure 7a. Although the details at the edges of each of these distributions are extracted with some uncertainty, the global features of these $P_i(E_T)$'s should be reliable.

TABLE 1: Properties of the H + NO_2 Product Channels

	E_{avail} (kcal/mol)	β	relative branching ratios	$\langle f_T\rangle^a$	$\langle f_{ele}\rangle$	$\langle f_{vib}\rangle^a$	$\langle f_{rot.}\rangle^a$
overall	70.4			0.30	0.44	0.26	
H + $NO_2(\tilde{X}^2A_1)$	70.4	~ 0	0.13	0.63		0.37	
H + $NO_2(\tilde{A}^2B_2)$	42.6	-0.4	0.21	0.74		0.22	0.04
H + $NO_2(\tilde{B}^2B_1)$	30.0	-0.2	0.66	0.44		0.56	
H + $NO_2(\tilde{C}^2A_2)$	27.9	-0.2		0.47		0.53	

[a] Fraction of energy is based on the E_{avail} of each product channel.

The overall $P(E_T)$ in Figure 7a indicates that a large amount of available energy is partitioned into internal energy of the NO_2 product (electronic, vibrational, and rotational). The overall average translational energy $\langle E_T\rangle = 0.30E_{avail}$. At least three electronic states of NO_2 are produced, with the higher $\tilde{B}$ and/or $\tilde{C}$ states mostly populated and an inverted electronic energy distribution. The vibrational state population in each of these NO_2 electronic states is highly inverted as well. $P(E_T)$'s are structureless in regions I and III, while in region II some vibrational structure is resolved. The relative branching ratios of these product channels are estimated on the basis of the areas of the $P_i(E_T)$ distributions in Figure 7a: $\tilde{X}^2A_1$:$\tilde{A}^2B_2$: $\tilde{B}^2B_1/\tilde{C}^2A_2$ $\approx$ 0.13:0.21:0.66. Note that $P(E_T)$ [obtained from $P_m(E_T)$] is the angle-integrated distribution and thus has been corrected for the different angular distributions of the product channels. The estimated errors of the branching ratios are in the order of 20% of the listed values. The summed results for these product channels are listed in Table 1.

Discussion

1. Electronically Excited States and Transition Moments of HONO. The 193.3-nm photoexcitation involves the second absorption band of HONO, which is due to the $\tilde{B}^1A' \leftarrow \tilde{X}^1A'$ transition via the $2a''(\pi_{nb,O}) \rightarrow 3a''[\pi^*(N{=}O)]$ excitation.[5a,7,9] The transition dipole moment $\boldsymbol{\mu}$ of this $\tilde{B} \leftarrow \tilde{X}$ transition is therefore in the molecular plane. The angle between $\boldsymbol{\mu}$ of the $\tilde{B} \leftarrow \tilde{X}$ transition and the dissociating N−O bond of HONO was calculated to be $\sim$39° (in the ground-state geometry of HONO, see Figure 8).[27] This angle has been confirmed by an experimental value in the range of 29−35° based on the vector correlations and Doppler profiles of OH LIF for the OH + NO channel by Vasudev et al.[26,27] For the H + NO_2 channels, the angle between the in-plane μ and the O−H bond direction is $\sim$63° based on the theoretical calculation (Figure 8). In the limit of prompt dissociation and axial recoil, the O−H bond direction is taken as the H atom recoil direction **v**, and the anisotropy parameter is expressed as $\beta = 2P_2(\cos\alpha)$, where α is the $\boldsymbol{\mu}$-**v** angle.[35] Thus, with a theoretical value $\alpha = 63°$, a β value of

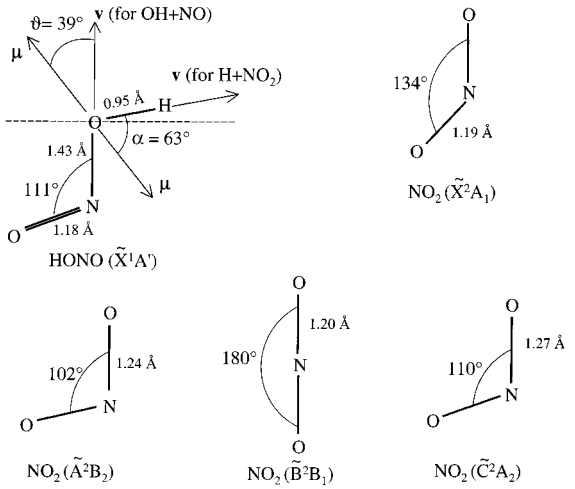

Figure 8. Equilibrium geometry of HONO($\tilde{X}^1A'$) (based on ref 38), $NO_2(\tilde{X}^2A_1)$, $NO_2(\tilde{A}^2B_2)$, $NO_2(\tilde{B}^2B_1)$, and $NO_2(\tilde{C}^2A_2)$ (based on refs 17 and 39). Bond length is in angstroms, and bond angle is in degrees. The transition dipole moment $\boldsymbol{\mu}$ of the $\tilde{B}^1A' \leftarrow \tilde{X}^1A'$ transition in HONO is indicated.

−0.38 is then derived. The experimental β values of −0.4 and −0.2 for region II and region III are consistent with the expectations, as discussed below. Note that if the HONO geometry and the α angle at the exit channel differ from those of the initial configuration, the β value will change accordingly, and in addition, when the dissociation process occurs at a longer time scale, β will become close to 0, giving a more isotropic angular distribution. For *cis*-HONO, assuming the same angle between $\boldsymbol{\mu}$ and the O−N bond, a β of ∼0.4 would be predicted for a prompt H + NO_2 channel, which is clearly not observed in the experiment.

The third singlet excited state ($\tilde{C}^1A''$) may be involved in the second absorption band as well. The transition dipole moment μ of the $\tilde{C} \leftarrow \tilde{X}$ transition is perpendicular to the molecular plane, and the β parameter should be −1 for a prompt dissociation.

2. H + $NO_2(\tilde{X}^2A_1)$ Channel. The first region of the $P(E_T)$ distribution in Figure 7a corresponds to production of the H + $NO_2(\tilde{X}^2A_1)$ fragments. Since H + $NO_2(\tilde{X}^2A_1)$ is the only possible product channel in the range of E_T = 43−70.4 kcal/mol, this assignment is unambiguous. The shape of this structureless peak (e.g., the slope around 43 kcal/mol in Figures 5a and 7a) does not appear to continue into the second region (the $\tilde{A}$ state of NO_2, with a resolved vibrational structure) or into the third region (the $\tilde{B}$ and/or $\tilde{C}$ state of NO_2). More importantly, the energy-dependent β parameter indicates that the $NO_2(\tilde{X}^2A_1)$ product has a different β from the $NO_2(\tilde{A}^2B_2)$ and $NO_2(\tilde{B}^2B_1)$ products (which are in the lower E_T region). Therefore, the contribution of the $\tilde{X}^2A_1$ state (peak I, Figure 7a) is concentrated in the region of 30−60 kcal/mol (i.e., not extended into or insignificant in the region below 30 kcal/mol where the $\tilde{B}$ and/or $\tilde{C}$ states start). Translational energy release of the $NO_2(\tilde{X}^2A_1)$ product channel is large (with $f_T \approx 0.63$). Vibrational population of $NO_2(\tilde{X}^2A_1)$, although not resolved, is clearly inverted. Conversely, the β value of ≥ 0 for the H + $NO_2(\tilde{X}^2A_1)$ channel seems to indicate a nearly isotropic product angular distribution.

Since the H + $NO_2(\tilde{X}^2A_1)$ channel is not correlated adiabatically with HONO($\tilde{B}^1A'$) in either coplanar or nonplanar geometries, production of the ground-state $NO_2(\tilde{X}^2A_1)$ requires nonadiabatic processes in HONO. One possibility is that the $\tilde{B}^1A'$ HONO could undergo internal conversion to the ground-state surface of HONO($\tilde{X}^1A'$), which has the same symmetry for vibronic couplings, and then dissociate to H + $NO_2(\tilde{X}^2A_1)$. Although the $\beta \geq 0$ might be consistent with unimolecular decomposition of HONO($\tilde{X}^1A'$) into H + $NO_2(\tilde{X}^2A_1)$ in a time scale longer than a rotational period, the large product translational energy release contradicts this mechanism. An alternative is that the excited $\tilde{B}^1A'$ HONO could undergo intersystem crossing to the $\tilde{b}^3A'$ state, which then dissociates into the H + $NO_2(\tilde{X}^2A_1)$ products. Ab initio calculation has identified a dissociation barrier along the H−ONO coordinate on the $\tilde{b}^3A'$ surface in the planar fragmentation geometry,[9] and thus the HONO dissociation, with enough energy provided by the 193.3-nm excitation, could have a repulsive translational energy release after passing this barrier. The β value of ≥0 for the H + $NO_2(\tilde{X}^2A_1)$ channel might then be due to a change of the initial geometry of HONO in going from the $\tilde{B}^1A'$ state to the $\tilde{b}^3A'$ state and the subsequent H-atom departure on the triplet surface via an exit-channel geometry with a $\boldsymbol{\mu}-\mathbf{v}$ angle of ∼55°.

The large vibrational excitation in NO_2 could be rationalized by the significant change in geometry between the HONO parent and the $NO_2(\tilde{X}^2A_1)$ product. Specifically, the ONO bond angle changes from the equilibrium value of 111° in the ground-state HONO[38] to 134° in $NO_2(\tilde{X}^2A_1)$.[17,39] Therefore, bending vibrational excitation in NO_2 is expected in going from the parent molecule [which determines the geometric structure of the Franck−Condon (FC) region on the excited-state HONO($\tilde{B}^1A'$)] to the product in a fast dissociation. With only the bending excitation considered, the peak internal energy of $NO_2(\tilde{X}^2A_1)$ corresponds to v_2 (bending vibration) ∼12 and an ONO bond angle of ∼107° at the classic turning point on the bending potential energy curve of $NO_2(\tilde{X}^2A_1)$.[17a,40] This result implies that the excited HONO parent has an effective ONO angle of 107°, consistent with the initial ONO bond angle of 111° in the FC region. The region where the excited states of HONO couple, as well as the exit channel, may differ from the FC configuration and require some change in the ONO angle. Finally, other vibrational modes of NO_2 could also be populated, which, along with a high rotational excitation, may account for the lack of resolved vibrational structure in the spectrum.

It is well-known that the $\tilde{X}^2A_1$ and $\tilde{A}^2B_2$ states of NO_2 are coupled by vibronic interactions via the asymmetric stretching mode, which results in a conical intersection of the $\tilde{X}^2A_1$ and $\tilde{A}^2B_2$ surfaces.[14,16,17,40−46] The vibronic coupling starts near the minimum of the $\tilde{A}^2B_2$ surface (9726 cm^{-1}, corresponding to E_T = 42.6 kcal/mol in this experiment), and increases gradually and selectively with energy up to 12 500 cm^{-1}, depending on the near resonance of the $\tilde{X}^2A_1$ and $\tilde{A}^2B_2$ zero-order levels and the coupling matrix element.[16,41,42] The vibronic coupling further increases above 12 500 cm^{-1}, but some regularities or clumps of the strongly mixed vibronic bands, which are mainly caused by $\tilde{A}^2B_2$ bending progression, are still present.[16,42] Above 16 000 cm^{-1}, the nonadiabatic coupling fully mixes the two electronic states, generating a chaotic spectrum.[42,43] In this experiment, another possibility of the production of $NO_2(\tilde{X}^2A_1)$ is via the vibronic coupling with the excited-state $NO_2(\tilde{A}^2B_2)$ fragment, which, based on its adiabatic correlation with HONO($\tilde{B}^1A'$) in the coplanar geometry, could be readily produced (discussed below). The coupling of the $\tilde{X}^2A_1$ and $\tilde{A}^2B_2$ states of NO_2 could be developed (in subpicosecond time scale)[44] before the H atom completely departs, and the H atoms can therefore sample the mixed $\tilde{X}^2A_1$ character in the H + $NO_2(\tilde{A}^2B_2)$ channel in final state interactions. However, since the vibronic coupling starts only above ∼9700 cm^{-1}, this plausible pathway requires an extensive energy transfer from the internal modes of the ONO

moiety to H-atom translation. Furthermore, since the vibronic coupling is weak in this low-energy region (with only ~10% of the highly excited vibrational levels in the $\tilde{X}^2A_1$ state coupled with the $\tilde{A}^2B_2$ state and with small mixing coefficients),[16a,42] the fraction of the $\tilde{X}^2A_1$ character due to coupling with $\tilde{A}^2B_2$ may not be significant in the $H + NO_2(\tilde{X}^2A_1)$ channel.

3. $H + NO_2(\tilde{A}^2B_2)$ Channel. As discussed previously, the second region corresponds to the formation of $H + NO_2(\tilde{A}^2B_2)$, which correlates adiabatically in the planar geometry with the HONO $\tilde{B}^1A'$ excited state.[9,14] The $H + NO_2(\tilde{A}^2B_2)$ channel has a pronounced anisotropy in the H-atom angular distribution (with $\beta = -0.4$). This experimental β parameter is in good agreement with the theoretical value of -0.38, which is based on the theoretical $\boldsymbol{\mu}-\mathbf{v}$ angle $\alpha = 63°$ and an assumption of prompt dissociation.[27] Note that the $\beta = -0.4$ is an upper limit due to the deconvolution procedures. The observed anisotropy favors a prompt dissociation mechanism in which HONO($\tilde{B}^1A'$) dissociates directly into the $H + NO_2(\tilde{A}^2B_2)$ fragments in a short time less than a rotational period. The translational energy release is large and repulsive [$f_T = 0.74$, based on E_{avail} of the $H + NO_2(\tilde{A}^2B_2)$ channel]. A dissociation barrier along the H−ONO coordinate on the $\tilde{B}^1A'$ surface (obtained in a planar geometry and without full optimization of the geometric structure along the reaction path) has been identified by the theoretical calculation.[9] The repulsive energy release is therefore consistent with this repulsive barrier along the O−H dissociation coordinate and with the large available energy from the 193.3-nm photon (which readily overpasses the barrier). In addition, the specific product vibrational state population (discussed below) is also in agreement with the prompt photodissociation mechanism. On the other hand, the $\tilde{B}^1A'$ state might have a nonplanar equilibrium geometry as suggested by Vasudev et al., due to the removal of the out-of-plane pπ electron on the OH oxygen atom and reduction of the lone pair repulsion.[26,27] Upon vertical excitation to the $\tilde{B}$ state, the OH moiety would undergo an out-of-plane motion toward the equilibrium configuration, generating significant excitation in the out-of-plane torsion ν_6.[26,27] In the nonplanar fragmentation geometries, the $H + NO_2(\tilde{A}^2B_2)$ channel does not correlate with HONO($\tilde{B}^1A'$), and thus nonadiabatic process such as hopping to the $\tilde{A}^1A''$ or $\tilde{b}^3A'$ surfaces is needed. However, the planar geometry may still be accessed periodically when the H atom oscillates in and out of the molecular plane, and the direct production of $H + NO_2(\tilde{A}^2B_2)$ channel can still occur under this condition. Indeed, our experimental results favor a direct dissociation mechanism for the $H + NO_2(\tilde{A}^2B_2)$ channel.

The internal (vibrational and rotational) energy distribution of the $NO_2(\tilde{A}^2B_2)$ product, $P(E_{int})$, is shown in Figure 9, which is obtained by using eq 5 and a shift of the electronic energy of $NO_2(\tilde{A}^2B_2)$. This distribution reveals some vibrational structure, which is similar to the bending progression (with an oscillatory structure at a spacing of ~740 cm^{-1}) of the $\tilde{A}^2B_2$ electronic state near the same energy region in the near-IR absorption spectrum of NO_2[17b,41] and the photoelectron detachment spectrum of NO_2^-.[46,47] As discussed before, the vibronic structures of the $\tilde{A}^2B_2$ state are deeply influenced by the conical intersection between the $\tilde{X}^2A_1$ and $\tilde{A}^2B_2$ states and by Fermi resonances in the $\tilde{A}^2B_2$ state. The Fermi resonances, due to the approximate 2:1:2 ratio in the three vibrational frequencies in the $\tilde{A}^2B_2$ state (symmetric stretch $\nu_1 \approx 1484$ cm^{-1}, bending $\nu_2 \approx 740$ cm^{-1}, and antisymmetric stretch $\nu_3 \approx 1500$ cm^{-1}), cause the polyad structure.[16,17,41,42] In the low-energy region up to 12 500 cm^{-1}, the vibronic interactions between $\tilde{X}^2A_1$ and $\tilde{A}^2B_2$ are weaker than the average vibronic spacing, and thus are localized and

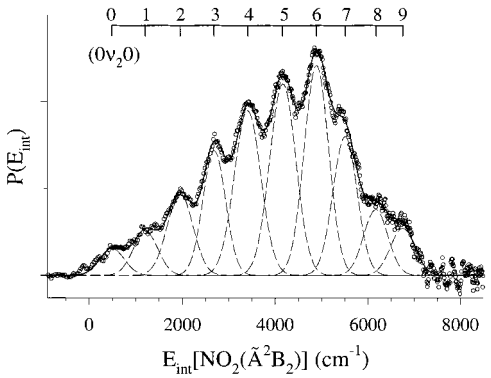

Figure 9. $NO_2(\tilde{A}^2B_2)$ internal energy distribution, $P(E_{int})$, from HONO photodissociation at 193.3 nm. This is obtained by conversion of the $NO_2(\tilde{A}^2B_2)$ peak in Figure 7a using eq 5 and a shift by the threshold energy of $NO_2(\tilde{A}^2B_2)$. The Gaussian peak fits of the NO_2 bending progression are plotted. Circles are experimental data, the solid line is the fitted spectrum, and dashed lines are Gaussian peaks whose widths include rotational envelopes and laser line width. The NO_2 bending progression is labeled in the figure.

can be treated *within* isolated polyads.[16,17,41,42] Therefore, the vibrational structures of $\tilde{A}^2B_2$ near the conical intersection are still regular and can be identified as polyads.[16,17b,41,42] In addition, $\tilde{A}^2B_2$ bending vibration has been shown to be the dominant character of the first couple of polyads (at a spacing of ~740 cm^{-1}) in the low-energy region.[16,17b,41,42] In this experiment, the resolution is in the order of 150 cm^{-1} (mainly due to the excitation laser line width), which does not allow resolution of the $\tilde{X}^2A_1$–$\tilde{A}^2B_2$ vibronic couplings with off-diagonal matrix elements in the order of 50 cm^{-1}.[16b,45,46] Therefore, a "zero-order" picture, in which the vibronic interactions of the $\tilde{X}^2A_1$ and $\tilde{A}^2B_2$ states are negligible, would be appropriate for the low-resolution $P(E_{int})$ distribution in the low-energy region near the origin of the $\tilde{A}^2B_2$ state. This is to say that, although the strong $\tilde{X}^2A_1$–$\tilde{A}^2B_2$ vibronic couplings and the vibrational couplings in the $\tilde{A}^2B_2$ state cause complex vibronic structures in the polyads, the low-resolution $P(E_{int})$ distribution in this experiment is not sensitive to these couplings that have small splittings and can only be detected with higher energy resolution.

To qualitatively model the vibrational population, $P(E_{int})$ in Figure 9 is deconvoluted by fitting with several Gaussian peaks, whose positions, heights, and widths are adjusted. Peak width is chosen to be nearly the same for all the peaks (~600 cm^{-1}). The peak width reflects the excimer photolysis laser line width, the rotational excitation in the NO_2 fragment, and the envelope of the perturbed vibrational levels. These peaks are evenly spaced (except the last three) with a separation of 735 ± 50 cm^{-1}, which is consistent with a bending progression based on the literature value of the bending frequency of $NO_2(\tilde{A}^2B_2)$.[16,17,41,42] The bending vibration of $NO_2(\tilde{A}^2B_2)$ is highly excited, with a maximum population of $\nu_2 = 6$ and an average internal energy of 11 kcal/mol. It is important to note that $P(E_{int})$ of $NO_2(\tilde{A}^2B_2)$ is extracted from the $P(E_T)$ distribution with some uncertainty, and the fitted vibrational distribution is qualitative and may not be unique. For example, possible ν_1 and ν_3 stretch excitations, which are due to the change of N−O bond length during the dissociation, may be buried in the $P(E_{int})$ and cannot be ruled out, and the Fermi resonances (with $\nu_1 \cong 2\nu_2 \cong \nu_3$) can further complicate the vibrational structures. Nevertheless, the main conclusion of a predominant bending progression that peaks around $\nu_2 = 6$ in the $NO_2(\tilde{A}^2B_2)$ product is robust.

The equilibrium ONO bond angle is 102° in the excited-state $NO_2(\tilde{A}^2B_2)$[17,39] and 111° in the ground-state HONO.[38] On the

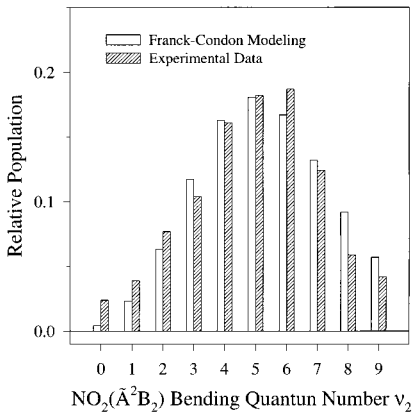

Figure 10. Franck−Condon modeling of the bending vibration excitation in $NO_2(\tilde{A}^2B_2)$. The shaded bars are the experimental bending vibration population, and the unfilled bars are for the Franck−Condon modeling. The total area of each of the two distributions is normalized to unity. See text for more details.

basis of the Franck−Condon principle, upon 193.3-nm photoexcitation, HONO on the $\tilde{B}^1A'$ surface is prepared with the same geometry as in the ground state, which is the starting point of the photodissociation of the exited-state HONO($\tilde{B}^1A'$). Vibrational excitation in the NO_2 bending mode is therefore expected from the change of the ONO angle in going from the parent molecule in the excited state to the product in a prompt dissociation. However, the change of the ONO angle between the initial geometry of the FC region on the $\tilde{B}^1A'$ surface (essentially the geometry of the equilibrium ground state) and $NO_2(\tilde{A}^2B_2)$ is not large enough to account for the extensive and inverted ONO bending progression. Additional change in the ONO bond angle while the O−H bond is dissociating is required to generate the observed bending progression. A simple one-dimensional Franck−Condon calculation (which considers only the NO_2 bending oscillator) has been carried out to model the observed bending progression. In this model, the ONO bending wave function of the excited-state HONO is projected onto the basis set of the bending vibration of $NO_2(\tilde{A}^2B_2)$, and under the assumption of a prompt and sudden dissociation, the $NO_2(\tilde{A}^2B_2)$ bending vibrational distribution can be obtained as the overlap integrals of the ONO bending vibrational wave function of the excited-state HONO and those of $NO_2(\tilde{A}^2B_2)$. The ONO bending modes of the excited-state HONO and $NO_2(\tilde{A}^2B_2)$ are represented by harmonic oscillators in the simulation. For the $NO_2(\tilde{A}^2B_2)$ bending, literature values of $\nu_2 \sim 740$ cm^{-1} and $\theta_{eq}(NO_2) = 102°$ are used. The ONO bond angle and bending frequency of the excited-state HONO configuration at which the H atom departs (or at the transition state) are assumed to be the equilibrium angle, θ_{eq}(O−N−O), and the frequency, ν, of the O−N−O bending harmonic oscillator potential in HONO. Note that, on the H−ONO part of the excited-state PES of HONO, the ONO moiety is bound. Both θ_{eq}(O−N−O) and ν of the excited-state HONO are optimized [with θ_{eq}(O−N−O) $= 120° \pm 1°$ and $\nu \approx 740 \pm 100$ cm^{-1}] to achieve the best fit of the experimental NO_2 bending progression (shown in Figure 10). Despite the crudeness of the simulation, the simple FC modeling indicates qualitatively that, starting from the FC region and determined by the topology of the excited-state PES, there is a potential gradient toward opening of the O−N−O bond angle, besides the force toward the O−H dissociation. This angular gradient creates a significant bending motion in the excited HONO, which is then carried into the NO_2 product while the excited HONO dissociates on the excited surface along the O−H coordinate. Specifically, the ONO angle is increased by ∼9° from the 111° at the FC region, and this enlarged ONO bond angle in HONO causes a more extensive bending excitation in the $NO_2(\tilde{A}^2B_2)$ (whose equilibrium angle is 102°) when the H atom departs. It is essential to point out that the FC modeling is to give a guideline for understanding the bending population, and in addition, the de-convolution and fitting of $P(E_{int})$ are affected by the associated uncertainties. Therefore, the ∼9° increase in the ONO angle has to be treated as a qualitative value. Nevertheless, the picture of a significant change of the ONO angle in the course of O−H bond dissociation is reliable. This conclusion is supported by examining the bending PES of $NO_2(\tilde{A}^2B_2)$:[17a,40] an O−N−O angle of ∼120° is required to produce a bending progression that peaks at $\upsilon_2 = 6$. An $NO_2(\tilde{A}^2B_2)$ bending progression peaking at $\upsilon_2 = 4$ in the photoelectron detachment spectrum of NO_2^-, in going from an equilibrium angle of 117.5° in NO_2^- to 102° in $NO_2(\tilde{A}^2B_2)$, also supports our Franck−Condon modeling and the conclusion of a significant change of O−N−O angle.[47] It seems that the effective $\boldsymbol{\mu}-\mathbf{v}$ angle α (between the O−H bond and $\boldsymbol{\mu}$) does not change significantly in the course of the dissociation, since the observed β parameter (−0.4) is in good agreement with the theoretical value (−0.38) based on the initial geometry of the FC region.[26,27] Finally, a decrease of the O−N−O angle in the excited-state HONO is also possible in the FC modeling, with θ_{eq}(O−N−O) ∼ 86° and a decrease of ∼25° from 111° in the FC region. The above discussion of the $NO_2(\tilde{A}^2B_2)$ vibrational distribution can be applied qualitatively as well. However, due to the modest O−N−O angle dependence of the 2a″ and 3a″ orbitals of HONO (in the 2a″ → 3a″ transition),[9,48] a large decrease of the O−N−O angle is unlikely (at least in the FC region).

4. H + $NO_2(\tilde{B}^2B_1)$ and/or $NO_2(\tilde{C}^2A_2)$ Channels. The thresholds of the H + $NO_2(\tilde{B}^2B_1)$ and H + $NO_2(\tilde{C}^2A_2)$ channels are $E_T = 30.0$ and 27.9 kcal/mol, respectively.[17] The third component in the $P(E_T)$ distribution in Figure 7a, starting in this region, should correspond to these two channels. This third component peaks at $E_T \sim 10$ kcal/mol and has an inverted vibrational population in $NO_2(\tilde{B}^2B_1)$/$NO_2(\tilde{C}^2A_2)$, although little vibrational structure is resolved (partially due to the poor *S*/*N* ratio). This high internal energy region corresponds to the well-known NO_2 vibrational chaos, which appears at internal energies above 45 kcal/mol (or $E_T < 24$ kcal/mol) and is caused by the strong $\tilde{X}^2A_1$–$\tilde{A}^2B_2$ vibronic coupling and the Fermi resonances in the $\tilde{A}^2B_2$ state.[16,42,43] In addition, the $\tilde{X}^2A_1$ and $\tilde{C}^2B_1$ states and the $\tilde{A}^2B_2$ and $\tilde{C}^2A_2$ states are coupled by Renner−Teller effect, respectively, and the $\tilde{B}^2B_1$ and $\tilde{C}^2A_2$ states could be coupled by vibronic coupling as well.[16,17] Although these couplings are in the free NO_2 molecules, it is possible that they start to occur (e.g., $\tilde{A}^2B_2 \rightarrow \tilde{X}^2A_1$ within 100 fs),[44] while the H-atom fragment is leaving but still interacting with the NO_2 moiety during the dissociation. The congestion of the $P(E_T)$ distribution in this region could be due to the strong mixings of the electronic states involved. A slightly anisotropic angular distribution in this region is observed with an average $\beta \approx -0.2$.

As the $NO_2(\tilde{B}^2B_1)$ correlates adiabatically in the planar geometry with the $\tilde{A}^1A''$ state and $\tilde{a}^3A''$ state of HONO, production of the $NO_2(\tilde{B}^2B_1)$ from the initially excited $\tilde{B}^1A'$ HONO requires nonadiabatic processes such as internal conversion from the $\tilde{B}^1A'$ surface to $\tilde{A}^1A''$ or intersystem crossing to $\tilde{a}^3A''$. The out-of-plane torsion excitation [$\upsilon_6(a'')$] in the $\tilde{B} \leftarrow \tilde{X}$ transition, as suggested by the previous study,[26,27] could facilitate the internal conversion from $\tilde{B}^1A'$ to $\tilde{A}^1A''$ with an A″ vibronic symmetry. Alternatively, in the nonplanar geometries, the $NO_2(\tilde{B}^2B_1)$ product correlates adiabatically with the

$\tilde{B}^1A'$ HONO. Consequently, direct production of the H + $NO_2(\tilde{B}^2B_1)$ channel could explain its dominant branching ratio. The equilibrium ONO angle in $NO_2(\tilde{B}^2B_1)$ is 180°, much larger than that in the HONO; thus a large amount of NO_2 bending excitation is expected. The slightly less-negative β value of −0.2 could reflect the lengthened lifetime of the coplanar dissociation process in going from the $\tilde{B}^1A'$ to $\tilde{A}^1A''$ or $\tilde{a}^3A''$ and then to the products. Alternatively, it could also indicate a different $\boldsymbol{\mu}-\mathbf{v}$ angle α (~59°) when the H atom departs in the H + $NO_2(\tilde{B}^2B_1)$ channel in the nonplanar dissociation.

At 193.3 nm, HONO could be excited to the $\tilde{C}^1A''$ state as well, which correlates directly to $NO_2(\tilde{C}^2A_2)$. A vertical transition to the $\tilde{C}^1A''$ state at 188 nm, as opposed to 213 nm to the $\tilde{B}^1A'$ state, has been estimated by Larrieu et al.[9] A considerable barrier for the H−O cleavage on the HONO($\tilde{C}^1A''$) surface is also indicated by the calculation.[9] As the transition moment of the $\tilde{C} \leftarrow \tilde{X}$ transition is perpendicular to the HONO molecular plane and thus perpendicular to the recoiling velocity of the H fragment, a negative β value of −0.2 is also consistent with dissociation from the $\tilde{C}$ state. However, the lifetime should be a significant fraction of the rotational period, as the β is smaller in value than the theoretical value of −1 for a prompt dissociation. Further experiment at a slightly longer wavelength where only the $\tilde{B}$ state is excited could separate the contributions of these two possible dissociation pathways.

5. Relative Branching Ratios of the H + NO_2 and the OH + NO Channels. The broad and structureless feature of the second absorption band of HONO indicates a short excited-state lifetime. The dissociation lifetime of the lower $\tilde{A}^1A''$ state of HONO into OH + NO has been shown to be in the order of ~100 fs. The dissociation time scale of HONO($\tilde{B}^1A'$) into OH + NO should be comparable, since HONO($\tilde{B}^1A'$) also correlates adiabatically with the OH + NO channel and, in particular, its PES curve along the N−O dissociation coordinate is steeper than the one correlating to HONO($\tilde{A}^1A''$).[9] The short HONO-($\tilde{B}^1A'$) lifetime (in femtoseconds) with respect to OH + NO dissociation is consistent with the observed anisotropic OH + NO product angular distribution by Vasudev et al.[26,27] The dissociation lifetimes of the H + NO_2 channels are in general less than or comparable to the rotational period (in the order of ~ps) based on the H-atom angular distribution. The potential barriers along the H−O dissociation coordinate on the excited-state surfaces, as well as the nonadiabatic processes involved in some H + NO_2 channels, may slightly hinder the O−H dissociation processes. The small signal intensities of the H + NO_2 channels observed in this experiment imply their smaller branching ratios compared to those of the OH + NO channels.

Among the H + NO_2 channels, the H + $NO_2(\tilde{A}^2B_2)$ channel (adiabatic in the planar geometry and nonadiabatic in the nonplanar geometries) is not dominant, while the H + $NO_2(\tilde{B}^2B_1)$ (nonadiabatic in planar and adiabatic in nonplanar) or H + $NO_2(\tilde{C}^2A_2)$ is the most important one, and the nonadiabatic channel H + $NO_2(\tilde{X}^2A_1)$ is also significant. The large branching ratio of H + $NO_2(\tilde{B}^2B_1)$ channel could be rationalized by a nonplanar dissociation mechanism, in which the HONO($\tilde{B}^1A'$) correlates adiabatically with H + $NO_2(\tilde{B}^2B_1)$. In addition, although the H + $NO_2(\tilde{A}^2B_2)$ channel correlates adiabatically with HONO($\tilde{B}^1A'$) in the planar geometry, this channel is Woodward−Hoffmann symmetry forbidden.[33] The individual molecular orbital symmetry of the NO_2 moiety in the excited-state HONO($\tilde{B}^1A'$) is a″a″ (2a″ → 3a″, involving two out-of-plane electrons), but it has to change into the a′a′ symmetry ($4b_2 \rightarrow 6a_1$, involving two in-plane electrons) in the $NO_2(\tilde{A}^2B_2)$ product through a double-substitution electronic rearrangement.[9,14,17,48] This could reduce the rate of the adiabatic H + $NO_2(\tilde{A}^2B_2)$ channel in the planar dissociation, and thus the nonadiabatic channels become competitive. A close examination of orbital correlations indicates that the excited orbitals of HONO($\tilde{B}^1A'$), 2a″ → 3a″, correlate with $1a_2 \rightarrow 2b_1$ orbitals in a higher excited-state $NO_2(2^2B_2)$ [...$(1a_2)^1(4b_2)^2(6a_1)^1(2b_1)^1$], while the $4b_2 \rightarrow 6a_1$ orbitals in $NO_2(\tilde{A}^2B_2)$ correlate with a higher state of HONO.[9,14,17,48] Since both correlations have A′ symmetry in the planar geometry, an avoided crossing will result. This avoided crossing between the Franck−Condon (molecular) region and the asymptotic (product) region would then cause the apparent barrier on the adiabatic potential surface connecting HONO($\tilde{B}^1A'$) and H + $NO_2(\tilde{A}^2B_2)$.[9,33] The barriers on other excited-state surfaces of HONO in the planar geometry could arise for the same reason.

Conclusions

The H-atom product channels in the photodissociation of HONO at 193.3 nm via the $\tilde{B}^1A'$ state have been observed for the first time. Product CM translational energy distribution and energy-dependent angular distribution indicate that the NO_2 products are formed in at least three different electronic states, with the fraction of the overall average product CM translational energy $\langle f_T \rangle$ being 0.30. The relative branching ratios of the different NO_2 electronic channels are estimated to be: $\tilde{X}^2A_1$:$\tilde{A}^2B_2$:$\tilde{B}^2B_1$/$\tilde{C}^2A_2$ ≈ 0.13:0.21:0.66.

The ground-state $NO_2(\tilde{X}^2A_1)$ could be produced in the nonadiabatic processes via a triplet state (e.g., $\tilde{b}^3A'$) or the $\tilde{X}^1A'$ state of HONO. The $NO_2(\tilde{X}^2A_1)$ product has a highly inverted vibrational population, which is likely due to the change of the ONO angle in the region of intersystem crossing or internal conversion between the different HONO electronic states and subsequent dissociation. The large product translational energy seems to favor the dissociation process from a triplet state that has a repulsive dissociation barrier along the O−H coordinate.

The $NO_2(\tilde{A}^2B_2)$ product shows a large bending vibration excitation (peaking at $v_2 = 6$), and a simple Franck−Condon modeling indicates a significant change of the ONO angle during dissociation. The observed anisotropy parameter in the product angular distribution is in agreement with the predicted value based on the known in-plane transition dipole moment and a prompt dissociation mechanism, which suggests a short excited $\tilde{B}^1A'$ state lifetime (less than one rotational period) with respect to the H + $NO_2(\tilde{A}^2B_2)$ dissociation. A large fraction of the available energy of this channel is partitioned into product translation. The H + $NO_2(\tilde{A}^2B_2)$ channel is produced via a direct dissociation, which could occur via the coplanar geometry in which H + $NO_2(\tilde{A}^2B_2)$ correlated adiabatically with HONO-($\tilde{B}^1A'$), or from the nonplanar geometries that occasionally sample the near-planar configurations.

The vibrational population of the $NO_2(\tilde{B}^2B_1)$ and/or $NO_2(\tilde{C}^2A_2)$ states is also inverted, and a small anisotropy of the H-atom product has been observed. The H + $NO_2(\tilde{B}^2B_1)$ channel could be produced by nonadiabatic processes via the $\tilde{A}^1A''$ or $\tilde{a}^3$ A″ surfaces of HONO in the coplanar fragmentation geometry. This channel could also be produced adiabatically from the HONO($\tilde{B}^1A'$) in the noplanar geometries, which is consistent with the large branching ratio of this channel. The H + $NO_2(\tilde{C}^2A_2)$ channel might involve the $\tilde{C}^1A''$ state of HONO.

Acknowledgment. This work is supported by National Science Foundation (Grant CHE-9811400) and partially by a UC Regents' Faculty Fellowships and Faculty Development Award, an ACS-PRF Type G Grant, and a Camille and Henry

Dreyfus New Faculty Award. We thank Prof. Curt Wittig for donating the excimer laser and a vacuum chamber used in this work. We thank the reviewers for their valuable comments.

References and Notes

(1) Finlayson-Pitts, B. J.; Pitts, J. N., Jr. *Chemistry of the Upper and Lower Atmosphere*; Academic Press: New York, 2000.

(2) Lammel, G.; Cape, J. N. *Chem. Soc. Rev.* **1996**, *25*, 361, and references cited therein.

(3) Jenkin, M. E.; Cox, R. A.; Williams, D. J. *Atmos. Environ.* **1988**, *22*, 487.

(4) (a) Winer, A. M.; Biermann, H. W. *Res. Chem. Intermed.* **1994**, *20*, 423. (b) Calvert, J. G.; Yarwood, G.; Dunker, A. M. *Res. Chem. Intermed.* **1994**, *20*, 463.

(5) (a) Cox, R. A.; Derwent, R. G.; *J. Photochem.* **1976**, *6*, 23. (b) Stockwell, W. R.; Calvert, J. G. *J. Photochem*. **1978**, *8*, 193. (c) Bongartz, A.; Kames. J.; Welter, F.; Schurath, U. *J. Phys. Chem*. **1991**, *95*, 1076. (d) Pagsberg, P.; Bjergbakke, E.; Ratajczak, E.; Sillesen, A.; *Chem. Phys. Lett.* **1997**, *272*, 383. (e) Vasudev, R. *Geophys. Res. Lett.* **1990**, *17*, 2153.

(6) Atkinson, R.; Baulch, D. L.; Cox, R. A.; Hampson, R. F., Jr.; Kerr, J. A.; Rossi, M. J.; Troe, J. *J. Phys. Chem. Ref. Data* **1997**, *26*, 1329.

(7) Kenner, R. D.; Rohrer, F.; Stuhl, F. *J. Phys. Chem.* **1986**, *90*, 2635.

(8) King, G. W.; Moule, D. *Can. J. Chem.* **1962**, *40*, 2057.

(9) Larrieu, C.; Dargelos, A.; Chaillet, M. *Chem. Phys. Lett.* **1982**, *91*, 465.

(10) Hennig, S.; Untch, A.; Schinke, R.; Nonella, M.; Huber, R. *Chem. Phys.* **1989**, *129*, 93.

(11) Suter, H. U.; Huber, J. R. *Chem. Phys. Lett.* **1989**, *155*, 203.

(12) Schinke, R.; Untch. A.; Suter, H. U.; Huber, J. R. *J. Chem. Phys.* **1991**, *94*, 7929.

(13) Cotting, R.; Huber, J. R. *J. Chem. Phys.* **1996**, *104*, 6208.

(14) Jackels, C. F.; Davidson, E. R. *J. Chem. Phys.* **1976**, *65*, 2941. The a_1 and b_2 orbitals are symmetric with respect to reflection in the NO_2 molecular (*yz*) plane and thus have *a*′ symmetry in the C_s point group, while the a_2 and b_1 orbitals have *a*″ symmetry. Note that in ref 9 the order and reduced symmetry of the $^2B_2$ and $^2B_1$ states in the C_s point group were inverted.

(15) (a) Chase, M. W., Jr. *NIST-JANAF Themochemical Tables*, 4th ed.; Journal of Physical ahd Chemical Reference Data, Monograph 9; American Chemical Society: Washington, DC, 1998. D_0(HO−NO) ($\Delta H_0°$ for **1a**) and D_0(H−ONO) ($\Delta H_0°$ for **2a**) are derived based on the $\Delta_f H°$ (0 K) values in the tables. (b) Huber, K. P.; Herzberg, G. *Molecular Spectra and Molecular Structure IV. Constants of Diatomic Molecules*; Van Nostrand: New York, 1979.

(16) (a) Kirmse, **B.;** Delon, A.; Jost, R. *J. Chem. Phys.* **1998**, *108*, 6638. The unperturbed electronic energy T_0 of $NO_2(\tilde{A}^2B_2)$ is 9726 ± 5 cm^{-1}. (b) Delon, A.; Jost, R. *J. Chem. Phys.* **1991**, *95*, 5686. (c) Delon, A.; Jost, R. *J. Chem. Phys.* **1999**, *110*, 4300.

(17) (a) Gillispie, G. D.; Khan, A. U.; Wahl, A. C.; Hosteny, R. P.; Krauss, M. *J. Chem. Phys.* **1975**, *63*, 3425. (b) Gillispie, G. D.; Khan, A. U. *J. Chem. Phys.* **1976**, *65*, 1624. (c) Hsu, D.; Monts, D.; Zare, R. N. *Spectral Atlas of Nitrogen Dioxide*; Academic Press: New York, 1978. The electronic energy T_0 (derived from theoretical T_e with zero point energy correction) is 1.75 eV for $NO_2(\tilde{B}^2B_1)$ and ∼1.84 eV for $NO_2(\tilde{C}^2A_2)$.

(18) Vasudev, R.; Zare, R. N.; Dixon, R. N. *Chem. Phys. Lett.* **1983**, *96*, 399.

(19) Vasudev, R.; Zare, R. N.; Dixon, R. N. *J. Chem. Phys.* **1984**, *80*, 4863.

(20) Novicki, S. W.; Vasudev, R. *J. Chem. Phys.* **1991**, *95*, 7269.

(21) Dixon, R. N.; Rieley, H. *Chem. Phys.* **1989**, *137*, 307.

(22) Dixon, R. N.; Rieley, H. *J. Chem. Phys.* **1989**, *91*, 2308.

(23) Shan, J. H.; Wategaonkar, S. J.; Vasudev, R. *Chem. Phys. Lett.* **1989**, *158*, 317.

(24) Holland, S. M.; Stickland, R. J.; Ashfold, M. N. R.; Newnham, D.; Mills, I. M. *J. Chem. Soc., Faraday Trans.* **1991**, *87*, 346.

(25) Burkholder, J. B.; Mellouki, A.; Talukdar, R.; Ravishankara, A. R. *Int. J. Chem. Kinet.* **1992**, *24*, 711.

(26) Novicki, S. W.; Vasudev, R. *Chem. Phys. Lett.* **1991**, *176*, 118.

(27) Wategaonkar, S. J.; Shan, J. H.; Vasudev, R. *Chem. Phys.* **1989**, *139*, 283.

(28) (a) Schnieder, L.; Meier, W.; Welge, K. H.; Ashfold, M. N. R.; Western, C. M. *J. Chem. Phys.* **1990**, *92*, 7027. (b) Ashfold, M. N. R.; Lambert, I. R.; Mordaunt, D. H.; Morley, G. P.; Western, C. M. *J. Phys. Chem*. **1992**, *96*, 2938.

(29) Zhang, J.; Dulligan, M.; Wittig, C. *J. Phys. Chem.* **1995**, *99*, 7446.

(30) (a) Zhang, J.; Xu, K.; Amaral, G. *Chem. Phys. Lett.* **1999**, *299*, 285. (b) Xu, K.; Amaral, G. Zhang, J. *J. Chem. Phys.* **1999**, *111*, 6271.

(31) Ning, C. L.; Pfab, J. *J. Phys. Chem.* **1997**, *101*, 6008.

(32) Marshall, G.; Midgley, D. *Anal. Chem*. **1982**, *54*, 1490.

(33) Myers, T. L.; Forde, N. R.; Hu, B.; Kitchen, D. C.; Butler, L. J. *J. Chem. Phys*. **1997**, *107*, 5361, and references cited therein.

(34) Okabe, H. *Photochemistry of Small Molecules*; John Wiley & Sons: New York, 1978.

(35) (a) Zare, R. N. *Mol. Photochem*. **1972**, *4*, 1. (b) Yang, S. C.; Bersohn, R. *J. Chem. Phys*. **1974**, *61*, 4400.

(36) (a) Wang, J. H.; Hsu, Y. T.; Liu, K. *J. Phys. Chem.* **1997**, *101*, 6593. (b) Wang, J. H.; Liu, K. *J. Chem. Phys.* **1998**, *109*, 7107.

(37) Lee, S. *J. Phys. Chem.* **1995**, *99*, 13380.

(38) Finnigan, D. J.; Cox, A. P.; Brittain, A. H. *J. Chem. Soc., Faraday Trans. 2* **1972**, *68*, 548.

(39) Kuchitsu, K. ed. *Structure of Free Polyatomic Molecules*; Springer-Verlag: Berlin, **1998**; pp 72−73, and references cited therein.

(40) Katagiri, H.; Shigeki, K. *J. Chem. Phys.* **1993**, *99*, 8805.

(41) Orphal, J.; Dreher, S.; Voigt, S.; Burrows, J. P.; Jost, R.; Delon, A. *J. Chem. Phys.* **1998**, *109*, 10217.

(42) (a) Leonardi, E.; Petrongolo, C. *J. Chem. Phys.* **1997**, *106*, 10066. (b) Leonardi, E.; Petrongolo, C.; Hirsch, G.; Buenker, R. J. *J. Chem. Phys.* **1996**, *105*, 9051.

(43) Delon, A.; Jost, R. *J. Chem. Phys.* **1991**, *95*, 5701.

(44) Santoro, F.; Petrongolo, C. *J. Chem. Phys.* **1999**, *110*, 4419.

(45) Lievin, J.; Delon, A.; Jost, R. *J. Chem. Phys.* **1998**, *108*, 8931.

(46) Delon, A.; Georges, R.; Kirmse, B.; Jost, R. *Faraday Discuss.* **1995**, *102*, 117.

(47) Weaver, A.; Metz, R. B.; Bradforth, S. E.; Neumark, D. M. *J. Chem. Phys.* **1989**, *90*, 2070.

(48) Rabalais, J. W.; McDonald, J. M.; Scherr, V.; McGlynn, S. P.; *Chem. Rev.* **1970**, *71*, 73.